

Supporting Information

Heterolytic Hydrogen Activation: Understanding Support Effects in Water-Gas Shift, Hydrodeoxygenation, and CO Oxidation Catalysis.

Nicholas C. Nelson and Janos Szanyi*

Institute for Integrated Catalysis, Pacific Northwest National Laboratory, Richland, WA 99352 (USA)

*corresponding author: janos.szanyi@pnnl.gov

Materials and Methods.

Reagents. Tetraaminepalladium(II) nitrate (Sigma 377384), cerium(III) nitrate hexahydrate (Sigma 202991), cerium(IV) oxide (Sigma 544841), magnesium(II) oxide (Sigma 342793), zirconium(IV) oxide (Sigma 230693), lanthanum(III) oxide (Sigma 199923), titanium(IV) oxide (Sigma 718467), silicon(IV) oxide (Sigma 214477), zinc oxide (Sigma 544906), and silicon carbide (Alfa Aesar A11337) were used as received. Gamma aluminum(III) oxide (Puralox SBA-200) was supplied by Sasol and used as received.

Catalyst Synthesis. The Pd/Al₂O₃, Pd/CeO₂, Pd/MgO, Pd/ZrO₂, Pd/La₂O₃, Pd/SiO₂, Pd/ZnO, and Pd/TiO₂ catalysts were synthesized through impregnation of the neat oxide with Pd(NH₃)₄(NO₃)₂ solution (10 wt. % in water). The Pd/CeO₂-Al₂O₃ catalyst was synthesized through impregnation of Pd/Al₂O₃ (1.0028 g) with aqueous Ce(NO₃)₃·6H₂O (0.3340 g, 0.7692 mmol). Most impregnated materials were calcined in air at 400 °C for 6 h using a 2 °C min⁻¹ ramp rate. The 2 wt. % Pd/Al₂O₃, Pd/CeO₂, and Pd/CeO₂-Al₂O₃ catalysts were calcined in air at 600 °C for 6 h at 2 °C min⁻¹.

Catalytic Testing. Reactions were conducted in a fixed bed tubular quartz reactor contained within a tube furnace. A thermocouple was placed into the bed to monitor temperature. Silicon carbide was used as a diluent in all reactions. The catalysts and SiC were sieved between 38-63 μm. In a typical reaction, 40 mg of catalyst was diluted with 40 mg of SiC and placed into the quartz tube. The gas feed composition was 5 % CO₂, 20 % H₂, and 75 % He with a total flow rate of 140 mL min⁻¹ (GHSV ≈ 1.3x10⁵ h⁻¹) vented to atmosphere. Below 375 °C, diffusion and mass transfer limitations were absent according to the Koros and Nowak¹ criterion (Figure S1). Light-off curves were obtained by introducing the reagent feed to the calcined catalyst at 150 °C for 5 min. The temperature was ramped in 25 °C intervals at 2.5 °C min⁻¹. After 10 min under isothermal conditions, the reactant stream was analyzed by GC. After an additional 5 min under isothermal conditions, the ramp process was repeated. Catalyst performance was assessed using an on-line Agilent 7890B GC with a Supelco Carboxen 1010 PLOT column, methanizer, and FID detector.

The GC was run under isothermal conditions (35 °C) for 25 min using He carrier (10 mL min⁻¹). The retention time of CO and CO₂ were 2.5 and 13.5 min, respectively, as determined using the pure gases. Conversion was defined as mole percent and calculated as moles of converted CO₂ per mole of starting CO₂ times 100 %. Selectivity was defined as mole percent and calculated as moles of product per mole of all products times 100 %. Conversion rates to specific products were calculated from conversion, catalyst mass (g), and CO₂ flow rate (μmol s⁻¹).

$$rate = \frac{(conversion) \times (selectivity) \times (CO_2 \text{ flow rate})}{catalyst \text{ mass}}$$

Operando Infrared and Mass Spectrometry. The catalyst was studied under differential conditions (i.e. conversion < 5 %) using a combined GC/MS/IR apparatus equipped with two-position/four-port gas switching valves.² Catalyst activity was assessed using an Agilent 7820A GC with a Supelco Carboxen 1010 PLOT column, methanizer, and TCD detector. The GC run started at 50 °C for 5 min, then ramped to 160 °C at 20 °C min⁻¹ and held for 6 min using He carrier (10 mL min⁻¹). Time constants for gas-phase product evolution during isotopic switching were assessed using an Extrel CMS mass spectrometer equipped with Merlin Automation Data System. The time resolution is 0.6 s. Identification of and time constants for surface adsorbed species were determined using a Bruker IFS/66S FTIR system equipped with rapid scan software and an external broadband mid-IR MCT detector. Rapid-scan spectra were recorded in double-sided/forward-backward mode with mirror velocity of 320 kHz, spectral resolution of 4 cm⁻¹, and 64 scans per spectrum. The time resolution under these settings was 4.38 s. For the *stoichiometric* reaction, a time resolution of 1.10 s was used by reducing the number of scans to 16. The spectra were collected in transmission mode and reported in absorbance to allow for quantitative assessment through Beer-Lambert law. Background spectra were collected under He flow at operating temperatures for all experiments unless otherwise stated. For determination of monodentate formate time constant, the background spectra were collected under CO₂+He flow for better peak resolution.

The Pd/CeO₂-Al₂O₃ catalyst (11.5 mg) was pressed onto a tungsten mesh and loaded into the sandwich reactor-cell.³ Prior to each reaction/experiment, unless otherwise stated, the catalyst was treated under O₂ flow at 350 °C for 0.5-1 h to remove possible surface contaminants and make measurements under identical catalyst composition. The system was allowed to equilibrate under steady-state reaction conditions for at least 1 h prior to performing any measurements. In a typical isotopic transient experiment, the gas feed composition was 2 % Ar, 5 % CO₂, 20 % H₂, and 73 % He with a total flow rate of 60 mL min⁻¹ vented to atmosphere. Argon was used as inert tracer to correct the time constant for gas-phase hold-up (4.1 ± 0.3 s).

The surface and gas-phase kinetic data are reported as the mean of 5 isotopic switches (i.e. ¹²CO₂ + H₂ + Ar ↔ ¹³CO₂ + H₂, which yields 10 data points), where errors represent standard deviation. For gas-phase ^{12/13}CO transients using MS, the contribution to m/z = 28, 29 from ^{12/13}CO₂ fragmentation was subtracted by measuring the 28:44 or 29:45 mass ratio under ^{12/13}CO₂-He flow prior to each experiment. The gas-phase CO transients were fit using OriginPro® software and the ExpDec2 function (i.e. $y = y_0 + A_1 e^{-k_1 x} + A_2 e^{-k_2 x}$). The formate transient curves were generated by monitoring the wavenumber intensities at 1590 (br-H¹²COO), 1545 cm⁻¹ (i.e. H¹³COO), and 1660 cm⁻¹ (i.e. H¹²COO), respectively. These bands were

chosen to minimize the contributions from overlapping peaks. All spectra used to determine the formate time constants were normalized at 2150 cm^{-1} . For formate interconversion/diffusion studies, the spectra were normalized at 1690 cm^{-1} . The activation barrier for rWGS over Pd/CeO₂-Al₂O₃ in the operando reactor ($69 \pm 1 \text{ kJ mol}^{-1}$, Figure S2) was indistinguishable from the plug flow reactor ($70 \pm 3 \text{ kJ mol}^{-1}$, Figure 1b), indicating the absence of mass-transfer limitations.

Hydrogen Adsorption Measurements. Hydrogen adsorption was performed in a Micromeritics AutoChem II instrument using H₂/Ar (10 % H₂). The Pd/CeO₂-Al₂O₃ catalyst (47.9 mg) was aged under flowing H₂/Ar at 300 °C for 12 h, followed by He for 2 h, and then O₂ for 2 h. Afterward, the catalyst was treated under flowing H₂/Ar for 1 h, followed by He purge for 2 h. Then quantitative pulses of H₂/Ar were administered to the catalyst until saturation. The catalyst was then treated under O₂ for 2 h. This procedure, beginning with H₂/Ar flow for 1 h, was repeated using various He purge times.

Energy Dispersive X-ray (EDX) Analysis. The scanning transmission electron microscopy (STEM) imaging and analysis was performed with an aberration-corrected JEOL-ARM200F instrument operated at 200 kV. The EDX analysis was performed with a JEOL Centurio high-collection angle silicon drift detector (100 mm²).

X-Ray Diffraction (XRD). The Pd/CeO₂-Al₂O₃ diffractogram was measured from 20 to 80 ° two-theta using a Panalytical X'Pert Bragg-Brentano diffractometer with Cu-K α radiation ($\lambda = 1.5418 \text{ \AA}$), a graphite post-diffraction monochromator, and variable divergence and anti-scatter slits (illuminated length= 10 mm). Data were collected with a step size of 0.04 degrees two-theta.

X-Ray Photoelectron Spectroscopy. XPS measurements were performed with a Physical Electronics Quantera Scanning X-ray Microprobe. This system uses a focused monochromatic Al K α X-ray (1486.7 eV) source for excitation and a spherical section analyzer. The instrument has a 32 element multichannel detection system. The X-ray beam is incident normal to the sample and the photoelectron detector is at 45° off-normal. High energy resolution spectra were collected using a pass-energy of 69.0 eV with a step size of 0.125 eV. For the Ag 3d_{5/2} line, these conditions produced a FWHM of $0.92 \text{ eV} \pm 0.05 \text{ eV}$. The binding energy (BE) scale is calibrated using the Cu 2p_{3/2} feature at $932.62 \pm 0.05 \text{ eV}$ and Au 4f_{7/2} at $83.96 \pm 0.05 \text{ eV}$. The sample experienced variable degrees of charging. Low energy electrons at ~1 eV, 20 μA and low energy Ar⁺ ions were used to minimize this charging. The sample was exposed to pre-treatment gases in a variable temperature reaction chamber attached to the instrument prior to analysis.

Determination of TOF. The turnover frequency (TOF) in Figure 3a was determined by synthesizing Pd/M_xO_y catalysts with different Pd loadings (0.025, 0.05, 0.1, 0.5, 2 wt. %) following the procedure outlined above (see 'catalyst synthesis'). The individual data points for each catalyst in Figure 3a correspond to the activity at 300 °C following the procedure used to obtain the light-off curves (see 'catalytic testing'). The apparent activation barriers for all catalysts tested are shown in Table S1. The curves were fit using OriginPro® software and the ExPLinear function (i.e. $y = p_1 e^{-\frac{x}{p_2}} + p_3 + p_4 x$).

Determination of K_{OH}. The equilibrium constant for hydroxyl formation (K_{OH}) in Figure 3b was determined by identifying the conditions needed to obtain a nearly constant CO formation rate ($\mu\text{mol s}^{-1}$) under standard operating conditions (i.e. 20 kPa H₂) for all catalysts. The convergence of the CO formation rate

was coarse-tuned by Pd loading and fine-tuned by adjusting the catalyst mass. All catalysts were conditioned under reaction conditions for ≥ 12 h to minimize deactivation during measurements. The Pd loadings and mass of the catalysts used in Figure 3b are: Pd/SiO₂ (2 wt. %, 41.1 mg); Pd/TiO₂ (0.05 wt. %, 40.0 mg); Pd/CeO₂ (0.05 wt. %, 40.0 mg); Pd/Al₂O₃ (0.5 wt. %, 46.7 mg); Pd/La₂O₃ (2 wt. %, 35.0 mg); Pd/ZrO₂ (0.5 wt. %, 45.5 mg); Pd/MgO (2 wt. %, 203.3 mg); Pd/ZnO (2 wt. %, 29.4 mg).

Steady-State Isotopic Transient Kinetic Analysis (SSITKA) Theory. We refer the reader to the literature for more in-depth discussions on this topic.^{4,5} In brief, the transient response of the old (P) and new (P*) isotopic label during a step-function input (P \rightarrow P*) is designated as F^P(t) and F^{*P}(t), respectively. For pseudo-first-order kinetics, rate = k[A], the solution for F^P(t) is:

$$F^P(t) = e^{-kt}$$

If two intermediates contribute to the rate in parallel, the solution for F^P(t) is a weighted summation of two exponentials:

$$F^P(t) = \phi_1 e^{-kt} + \phi_2 e^{-kt}$$

$$\phi_1 + \phi_2 = 1$$

The isotopic response for species P can be attributed to the residence time on the catalyst surface during reaction. That is, integration of the normalized step-decay, F^P(t), or step-input, F^{*P}(t), response yields the overall mean surface residence time (τ) of all adsorbed surface intermediates that lead to P.

$$\tau^P = \int_0^{\infty} F^P(t) dt = \int_0^{\infty} [1 - F^{*P}(t)] dt$$

The number surface intermediates (N_p) on the catalyst surface that lead to product P is obtained using the mean residence time and the steady-state formation rate (r_p) of species P.

$$N_p = r_p \tau^P$$

Thus, SSITKA permits a direct and separate measurement for the abundance of surface intermediates (N_p) and the reactivity ($\tau = k^{-1}$) during reaction at steady-state (i.e. constant rate and coverage). The turnover frequency (TOF_P), steady-state reaction rate (r_p), and pseudo-first-order rate constant (k) for product P are related below.

$$TOF_P = \frac{r_p}{N_T} = k \frac{N_p}{N_T} = k \theta_T^P = \frac{1}{\tau^P} \theta_T^P$$

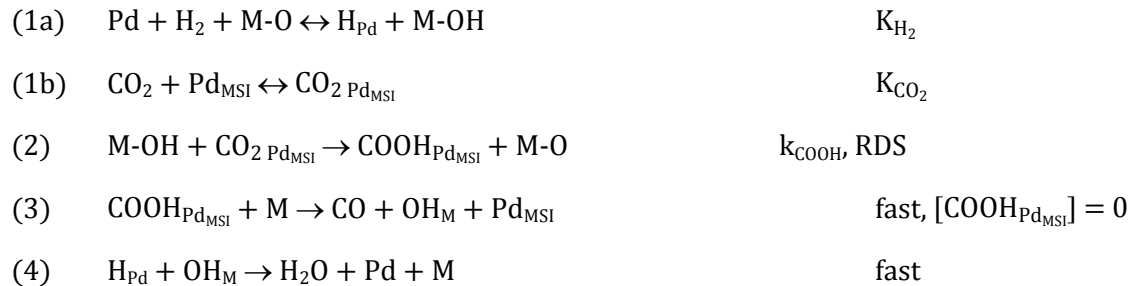
where N_T is the total number of catalyst active sites and θ_T^P is the fractional coverage of species P (i.e. $\frac{N_p}{N_T}$).

Coupling the SSITKA technique with IR spectroscopy provides a means to determine if a relationship exists between gas-phase and surface species. That is, the time constants derived from gas-phase products and surface species can be directly compared in the absence of chromatographic effects. If they are equal, it can be concluded that the surface specie is a precursor to the gas-phase product.

Derivation of rate law

Elementary Reaction Steps*

*We have neglected the formate pathway from Scheme 1 using this derivation since it is a minor contributor to the overall rate.



Overall Reaction:



Rate Law:

$$v = k_{\text{COOH}}[\text{M-OH}][\text{CO}_2 \text{Pd}_{\text{MSI}}]$$

Site Balance:

$$[\text{Pd}_{\text{MSI}}]_{\text{T}} = [\text{Pd}_{\text{MSI}}] + [\text{CO}_2 \text{Pd}_{\text{MSI}}] + [\text{COOH}_{\text{Pd}_{\text{MSI}}}] = [\text{Pd}_{\text{MSI}}] + [\text{CO}_2 \text{Pd}_{\text{MSI}}]$$

$$[\text{M-O}]_{\text{T}} = [\text{M-O}] + [\text{M-OH}]$$

Solve for [M-O] and [Pd_{MSI}]:

$$K_{\text{H}_2} = \frac{[\text{H}_{\text{Pd}}][\text{M-OH}]}{P_{\text{H}_2}[\text{Pd}][\text{M-O}]}$$

$$K_{\text{OH}} = \frac{[K_{\text{H}_2}][\text{Pd}]}{[\text{H}_{\text{Pd}}]} = \frac{[\text{M-OH}]}{P_{\text{H}_2}[\text{M-O}]} \text{ assuming equilibration of [Pd] and [H}_{\text{Pd}}]$$

$$K_{\text{CO}_2} = \frac{[\text{CO}_2 \text{Pd}_{\text{MSI}}]}{P_{\text{CO}_2}[\text{Pd}_{\text{MSI}}]}$$

$$[\text{M-O}] = \frac{[\text{M-OH}]}{K_{\text{OH}}P_{\text{H}_2}}$$

$$[\text{Pd}_{\text{MSI}}] = \frac{[\text{CO}_2 \text{Pd}_{\text{MSI}}]}{P_{\text{CO}_2}K_{\text{CO}_2}}$$

Substitute into Site Balance:

$$[\text{Pd}_{\text{MSI}}]_{\text{T}} = \left(\frac{1 + K_{\text{CO}_2}P_{\text{CO}_2}}{K_{\text{CO}_2}P_{\text{CO}_2}} \right) [\text{CO}_2 \text{Pd}_{\text{MSI}}]$$

$$[\text{M-O}]_{\text{T}} = \left(\frac{1 + K_{\text{OH}}P_{\text{H}_2}}{K_{\text{OH}}P_{\text{H}_2}} \right) [\text{M-OH}]$$

Solve for Rate Law Terms:

$$[\text{CO}_2 \text{Pd}_{\text{MSI}}] = \frac{K_{\text{CO}_2} P_{\text{CO}_2} [\text{Pd}_{\text{MSI}}]_{\text{T}}}{1 + K_{\text{CO}_2} P_{\text{CO}_2}}$$

$$[\text{M} - \text{OH}] = \frac{K_{\text{OH}} P_{\text{H}_2} [\text{M} - \text{O}]_{\text{T}}}{1 + K_{\text{OH}} P_{\text{H}_2}}$$

Overall Rate Law:

$$v = \frac{k_{\text{COOH}} K_{\text{OH}} K_{\text{CO}_2} P_{\text{H}_2} P_{\text{CO}_2} [\text{Pd}_{\text{MSI}}]_{\text{T}} [\text{M} - \text{O}]_{\text{T}}}{(1 + K_{\text{OH}} P_{\text{H}_2})(1 + K_{\text{CO}_2} P_{\text{CO}_2})}$$

$$[1] = [\text{Pd}_{\text{MSI}}]_{\text{T}} [\text{M} - \text{O}]_{\text{T}}$$

$$v = \frac{k_{\text{COOH}} K_{\text{OH}} K_{\text{CO}_2} P_{\text{H}_2} P_{\text{CO}_2} [1]}{(1 + K_{\text{OH}} P_{\text{H}_2})(1 + K_{\text{CO}_2} P_{\text{CO}_2})}$$

Double Reciprocal Rate Law:

$$\frac{1}{v} = \frac{1}{k'_{\text{obs}} K_{\text{OH}} [1]} \left(\frac{1}{P_{\text{H}_2}} \right) + \frac{1}{k'_{\text{obs}} [1]}$$

$$k'_{\text{obs}} = \frac{k_{\text{COOH}} K_{\text{CO}_2} P_{\text{CO}_2}}{(1 + K_{\text{CO}_2} P_{\text{CO}_2})}$$

Rate Law Ratio for H₂ (H) and D₂ (D):

$$\frac{v_{\text{H}}}{v_{\text{D}}} = \left(\frac{k_{\text{COOH}}}{k_{\text{COOD}}} \right) \left(\frac{K_{\text{OH}} (1 + K_{\text{OH}} P_{\text{H}_2})^{-1}}{K_{\text{OD}} (1 + K_{\text{OD}} P_{\text{D}_2})^{-1}} \right)$$

$$\left(\frac{K'_{\text{OH}}}{K'_{\text{OD}}} \right) = \left(\frac{K_{\text{OH}} (1 + K_{\text{OH}} P_{\text{H}_2})^{-1}}{K_{\text{OD}} (1 + K_{\text{OD}} P_{\text{D}_2})^{-1}} \right)$$

$$\frac{v_{\text{H}}}{v_{\text{D}}} = \left(\frac{k_{\text{COOH}}}{k_{\text{COOD}}} \right) \left(\frac{K'_{\text{OH}}}{K'_{\text{OD}}} \right)$$

Supplementary Figures.

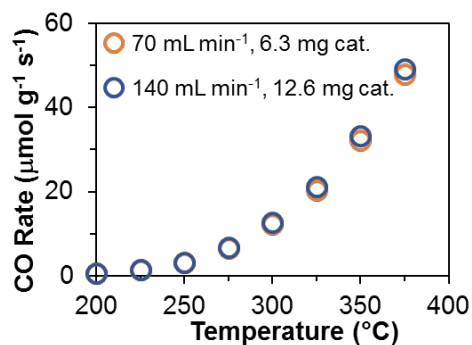


Figure S1. Mass transfer diagnostic test under plug-flow conditions for Pd/CeO₂-Al₂O₃ using the Koros and Nowak criterion.¹ The identical rates observed here indicate the reaction lies within the kinetic regime and no mass transfer limitations exist. The legend indicates the gas flow rate and the mass of catalyst. Silicon carbide was used to bring the total bed volume to 0.065 mL for each reaction.

Table S1. Apparent activation energies (kJ mol⁻¹) for selected catalysts during rWGS.

Pd wt. %	Pd/Al ₂ O ₃	Pd/CeO ₂	Pd/La ₂ O ₃	Pd/MgO	Pd/SiO ₂	Pd/TiO ₂	Pd/ZrO ₂	Pd/ZnO
2	72	63	83	72	77	54	75	73
0.5	68	63	80	104	77	65	84	73
0.1	74	65	90	82	81	69	74	77
0.05	75	72	96	93	77	63	73	81
0.025	74	76	107	85	79	63	80	78
	72 ± 3	68 ± 6	91 ± 11	87 ± 12	78 ± 2	63 ± 6	77 ± 5	76 ± 4
	77 ± 11							

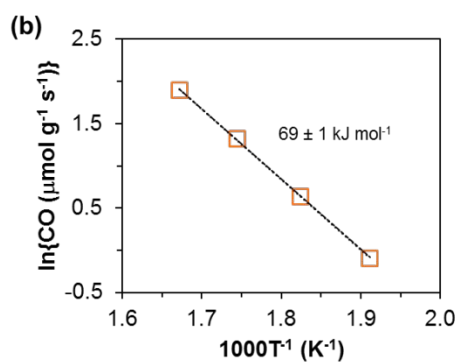
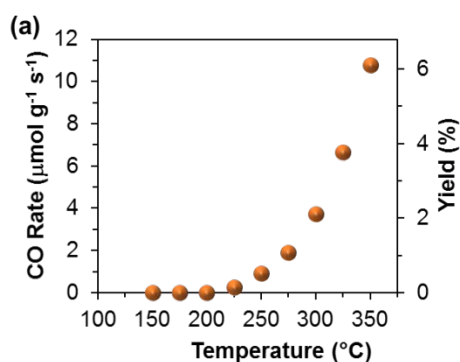


Figure S2. (a) CO₂ hydrogenation light-off curve for Pd/CeO₂-Al₂O₃ in operando reactor. (b) Corresponding Arrhenius plot and apparent activation barrier. Conditions: Pd/CeO₂-Al₂O₃ = 11.5 mg, flow rate = 60 mL min⁻¹, CO₂:4H₂:15He.

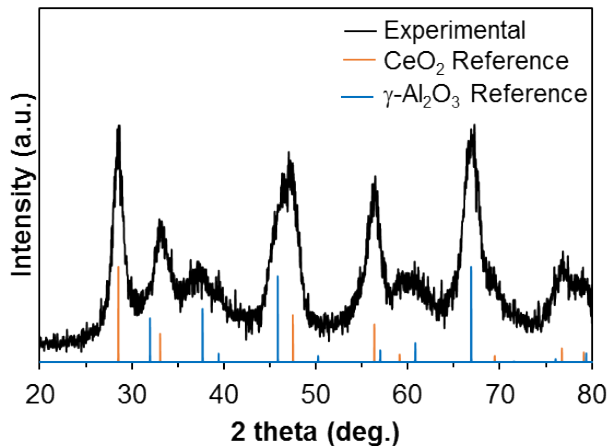


Figure S3. PXRD pattern for Pd/CeO₂-Al₂O₃ catalyst. Also shown are references for cubic ceria (CeO₂) and γ -alumina (γ -Al₂O₃). Crystallite size (\sim 6 nm) estimates are derived from the Scherrer equation.

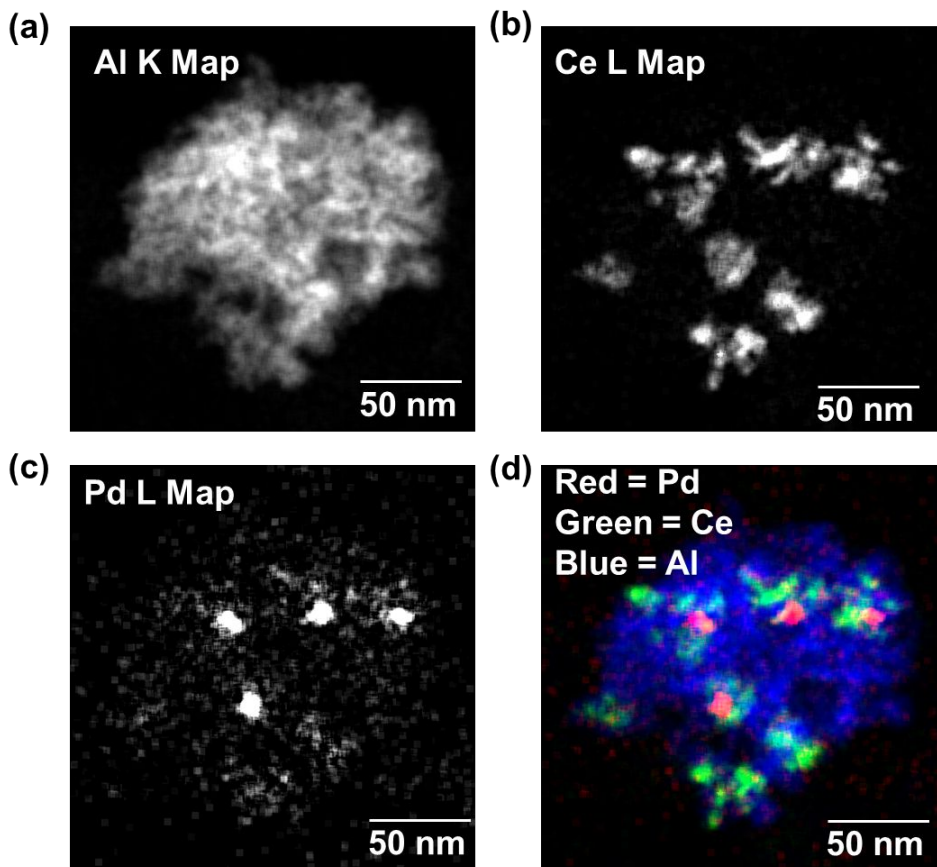


Figure S4. Energy dispersive X-Ray (EDX) maps corresponding to (a) Al, (b) Ce, (c) Pd, and (d) a false-coloring overlay of all three signals.

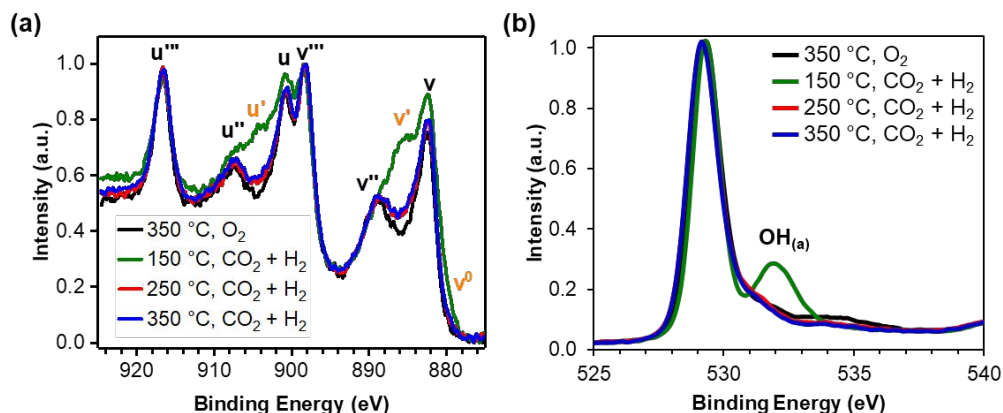


Figure S5. XPS spectra of Pd/CeO₂-Al₂O₃ in the (a) Ce 3d and (b) O 1s region after treatment with O₂ for 0.5 h at 350 °C and CO₂:4H₂:15He for 0.5 h at 150, 250, and 350 °C. The reactant feed was purged with He prior to cooling for transfer into XPS chamber. The sample was treated in O₂ for 0.5 h at 350 °C after each exposure to CO₂/H₂/He. The u', v', v⁰ labels (orange) correspond to Ce³⁺, while those in black correspond to Ce⁴⁺. The peak around 532 eV in (b) is attributed to surface hydroxyl.

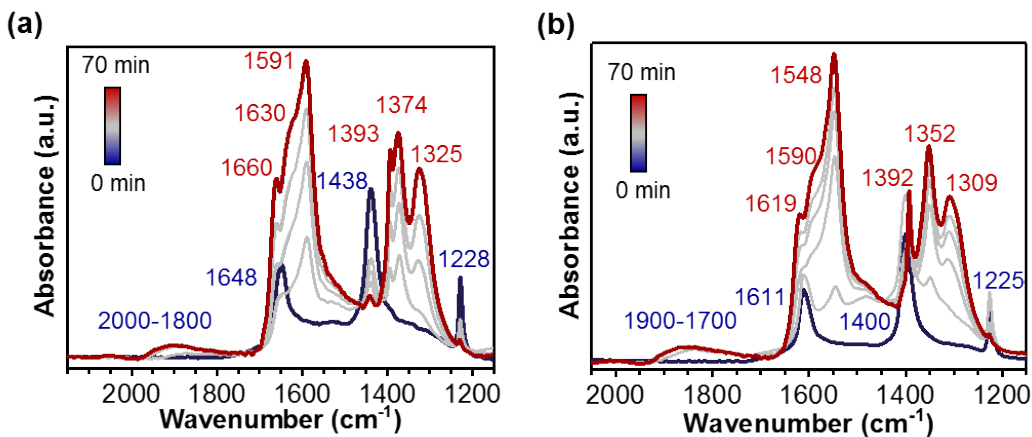


Figure S6. IR spectra recorded at 150 °C while flowing ¹²CO₂ (t = 0 min) and ¹²CO₂/H₂ (t > 0 min) over Pd/CeO₂-Al₂O₃. Bicarbonate bands appear at 1648 [ν(OCO)_{asym}], 1438 [ν(OCO)_{sym}], and 1228 [γ(COH)] cm⁻¹.^{6,7} Formate bands are observed at 1660 [ν(OCO)_{asym-mono}], 1630 [ν(OCO)_{asym-mono}], 1591 [ν(OCO)_{asym-br}], 1393 [δ(CH)], 1374 [ν(OCO)_{sym-br}], and 1325 [ν(OCO)_{sym-mono}] cm⁻¹.⁸⁻¹⁰ Carbonyl bands are observed from 2000-1800 [ν(CO)]. (b) IR spectra recorded at 150 °C while flowing ¹³CO₂ (t = 0 min) and ¹³CO₂/H₂ (t > 0 min) over Pd/CeO₂-Al₂O₃. Band assignments are analogous to those in (a). Conditions: CO₂:4H₂:15He, flow rate = 60 mL min⁻¹.

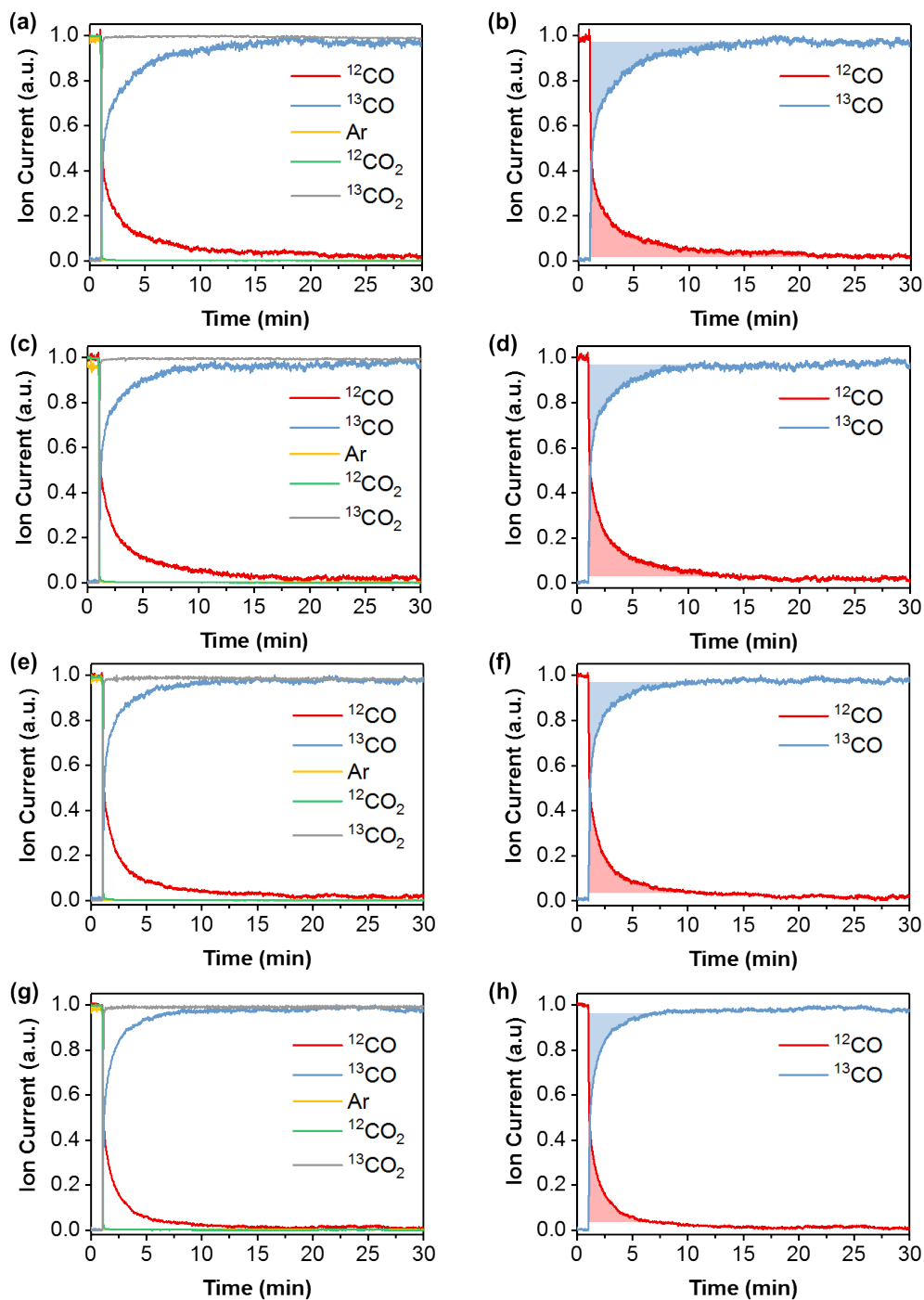


Figure S7. Representative MS data recorded during isotopic switching ($t = 1$ min) from $^{12}\text{CO}_2/\text{H}_2/\text{He}/\text{Ar}$ to $^{13}\text{CO}_2/\text{H}_2/\text{He}$ at (a-b) 275 °C, (c-d) 290 °C, (e-f) 300 °C, and (g-h) 325 °C. Figures (b, d, f, h) show the integrated area for ^{12}CO and ^{13}CO used to calculate the time constants reported in Table 1. Conditions: Pd/CeO₂-Al₂O₃ = 11.5 mg, flow rate = 60 mL min⁻¹, Ar = 2 %, CO₂ = 5 %, H₂ = 20 %, He = 73 %.

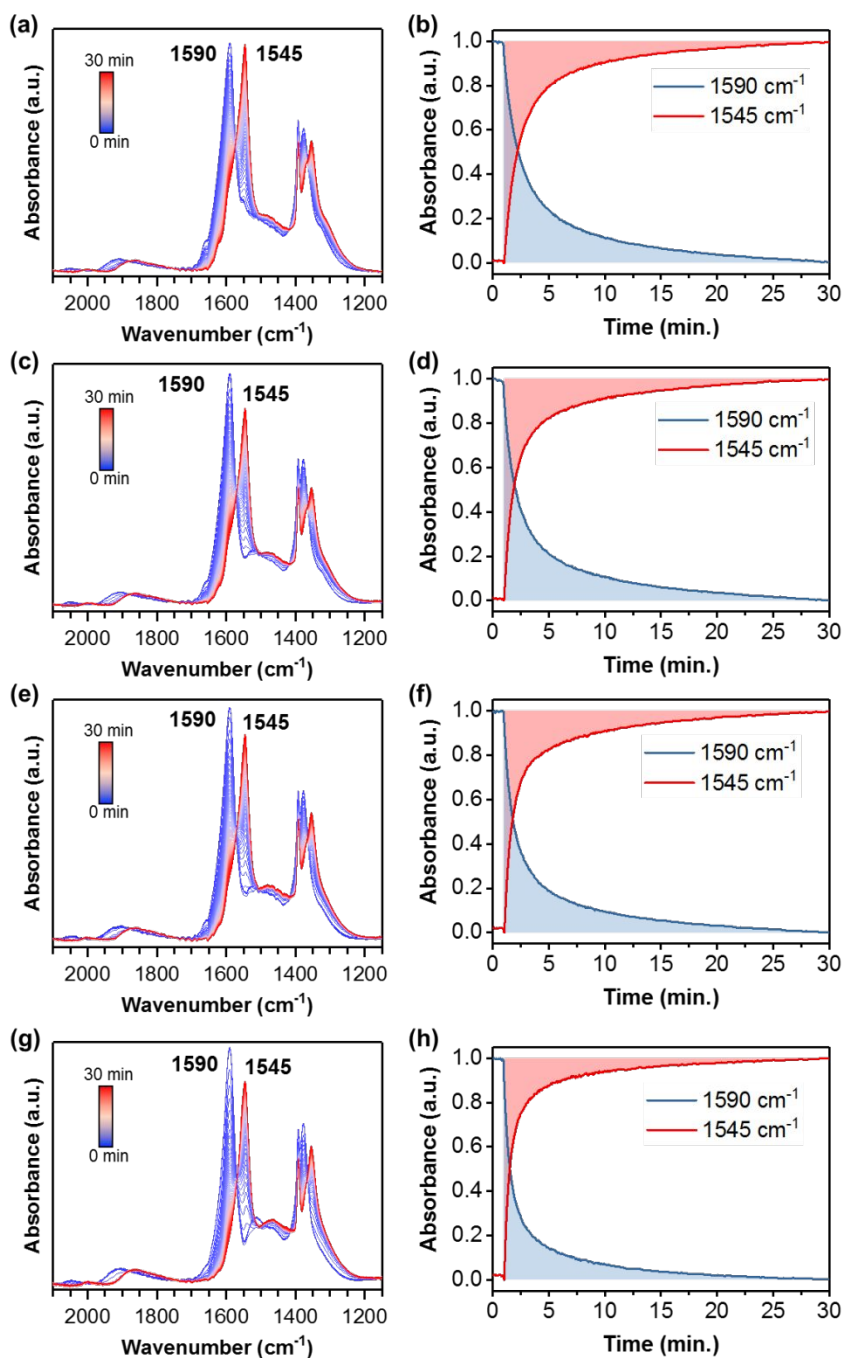


Figure S8. Representative IR spectra during isotopic switching ($t = 1$ min) from $^{12}\text{CO}_2/\text{H}_2/\text{He}/\text{Ar}$ to $^{13}\text{CO}_2/\text{H}_2/\text{He}$ at (a, b) 275 °C, (c, d) 290 °C, (e, f) 300 °C, and (g, h) 325 °C. Figures (b, d, f, h) show the integrated area for the band at 1590 cm⁻¹ (br-H¹²COO) and 1545 cm⁻¹ (br-H¹³COO) used to calculate the bridge formate time constants in Table 1. Conditions: Pd/CeO₂-Al₂O₃ = 11.5 mg, flow rate = 60 mL min⁻¹, Ar = 2 %, CO₂ = 5 %, H₂ = 20 %, He = 73 %.

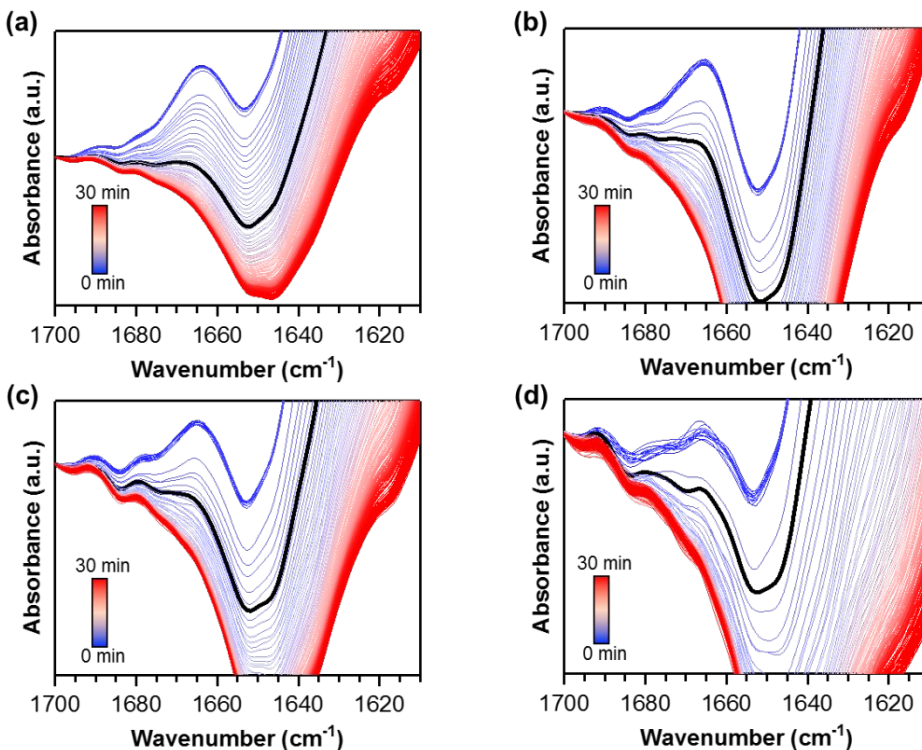


Figure S9. IR spectra collected during isotopic switching ($^{12}\text{CO}_2/\text{H}_2/\text{He}/\text{Ar} \rightarrow ^{13}\text{CO}_2/\text{H}_2/\text{He}$) at (a) 275 °C, (b) 290 °C, (c) 300 °C, and (d) 325 °C. Conditions are the same as in Figure S8. The spectra were collected using the background recorded under CO_2+He flow at steady-state. This allows for improved resolution of the monodentate formate band and more accurate kinetic analysis. The black traces represent the point at which the monodentate formate concentration goes to zero. That is, the black traces correspond to the upper time limit of integration used to determine the time constant.

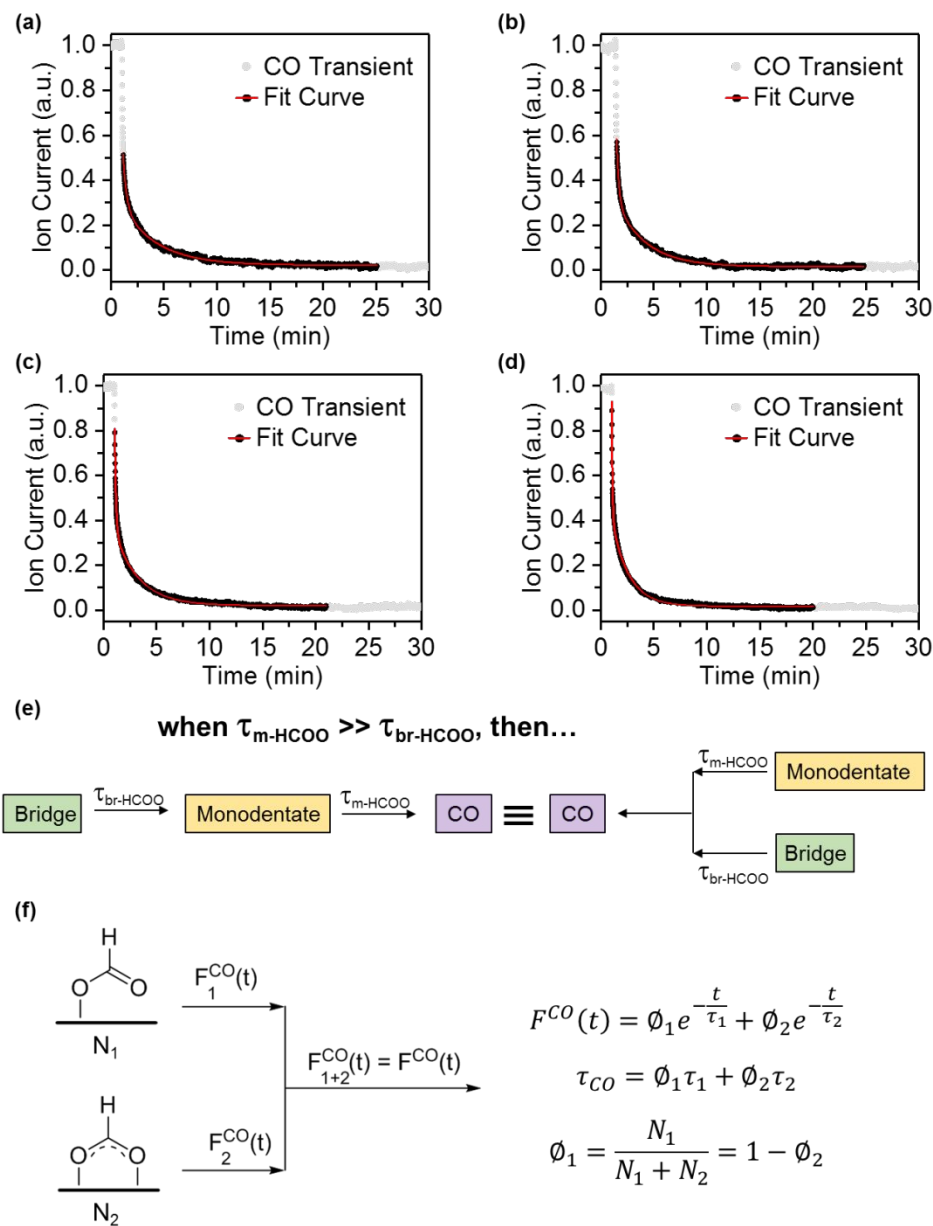


Figure S10. The MS-derived CO isotopic transient curves from isotopic switching experiments (Figure S7) at (a) 275 °C, (b) 290 °C, (c) 300 °C, and (d) 325 °C were fit using a linear combination of two exponential decay curves. The fitting parameters are compiled below in Table S2. (e) From our previous¹¹ and current results (vide infra), we know that formates follow a serial pathway: bridge formate diffuses to monodentate sites, followed by apparent dehydroxylation. This appears to contradict fitting the transient curves using a linear combination of two exponential curves, which is the solution for a parallel pathway (i.e., the solution for a serial pathway differs from a parallel pathway).⁴ However, the order of magnitude difference between τ_{m-HCOO} and $\tau_{br-HCOO}$ (Table 1) yields an apparent parallel pool reaction network for the following reason: The concentration of the monodentate formate isotopologue decreases fast upon isotopic switching, whereas the bidentate formate isotopologue decreases much more slowly. The order of magnitude difference in rates translates to an order of magnitude difference in surface concentration (i.e. IR-MS signal). Thus, we are unable to detect the bridge formate pool transiently feeding into the

monodentate formate pool prior to apparent dehydroxylation. If we were able to detect this serial event there would be a distinct transient profile that could not be fit with the parallel pathway equation.⁴ (f) Parallel pathway kinetics are needed to extract kinetic parameters (i.e. τ_i , N_i , ϕ_i) for each formate (monodentate and bridge) contributing to the CO isotopic transient curve ($F^{\text{CO}}(t)$).

As the CO transient temperature increases (a→d), a correspondence between the extracted gas-phase CO time constants (τ_1 and τ_2) and the formate time constants ($\tau_{\text{m-HCOO}}$ and $\tau_{\text{br-HCOO}}$) is only achieved by beginning the fit at progressively higher ion currents. A plausible reason is that at low temperatures, we are able to detect a contribution from the carboxyl pathway to the CO transient profile. As the temperature increases, the rate constant for the carboxyl pathway increases. Thus, in (d) the carboxyl rate is so much faster than the MS response time it essentially contributes nothing to the transient profile. Along the same reasoning, the monodentate formate is reacting progressively faster at each temperature. Thus, a larger portion of the transient curve is needed to achieve a correspondence between τ_1 and $\tau_{\text{m-HCOO}}$ (Table 1). Stated another way, at low temperatures the CO transient profile contains contributions from the carboxyl and formate intermediate, while at higher temperatures the CO transient profile only contains contributions from the formate intermediate. Fortunately, it is important to note that this explanation was written prior to collecting the data in Table 2. The time constant in Table 2 is $\tau_{\text{COOH}} = 4.5 \pm 0.3$ s at 300 °C. This value is equal to the time constant for the Ar tracer (4.1 ± 0.3 s), which represents the mean time for physically removing a non-interacting gas from the system. The τ_{COOH} value at 300 °C fully supports the need to begin the fit at progressively higher ion currents as the temperature increases since τ_{COOH} is inversely proportional to temperature.

Table S2. Kinetic parameters for Pd/CeO₂-Al₂O₃ obtained via fitting CO transient curves.

Temperature (°C)	τ_1 (s)	τ_2 (s)	N_1 ($\mu\text{mol g}^{-1}$)	N_2 ($\mu\text{mol g}^{-1}$)	ϕ_1	ϕ_2
275	21 ± 1	199 ± 6	110 ± 8	64 ± 5	0.68 ± 0.02	0.32 ± 0.02
290	14 ± 1	157 ± 10	117 ± 12	63 ± 6	0.69 ± 0.03	0.31 ± 0.03
300	8 ± 1	130 ± 7	116 ± 11	54 ± 5	0.70 ± 0.03	0.30 ± 0.03
325	5 ± 2	97 ± 3	129 ± 15	53 ± 6	0.72 ± 0.02	0.28 ± 0.02

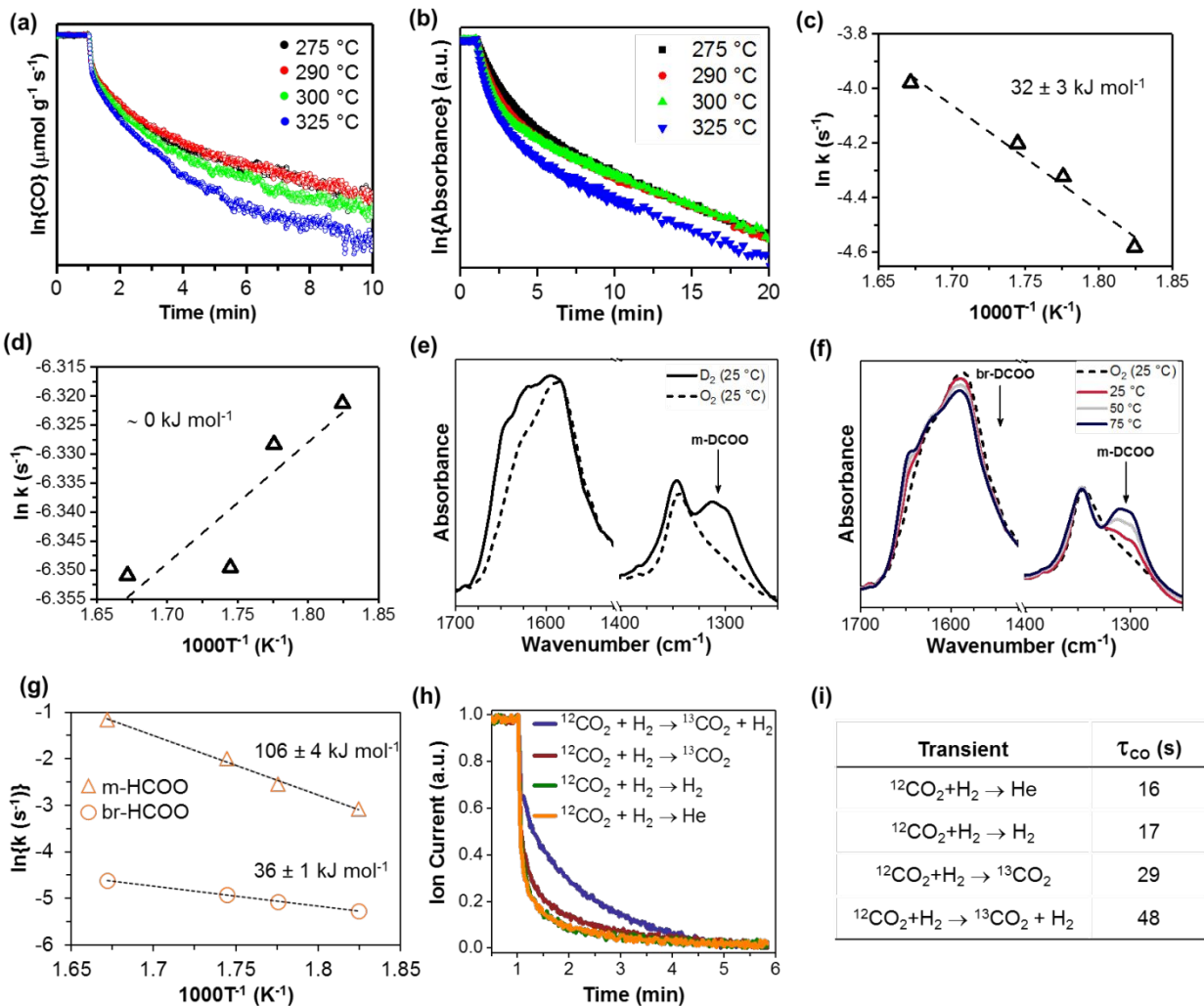


Figure S11. (a) Semilogarithmic CO transient curves obtained during isotopic switching experiments ($^{12}\text{CO}_2/\text{H}_2/\text{He}/\text{Ar} \rightarrow ^{13}\text{CO}_2/\text{H}_2/\text{He}$) are nonlinear indicating rWGS over Pd/CeO₂-Al₂O₃ cannot be described by only one active intermediate.⁴ The non-linearity results from both monodentate and bridge formate contributing to the transient curve.¹¹ (b) Semilogarithmic bridge formate transient curves obtained during isotopic switching experiments ($^{12}\text{CO}_2/\text{H}_2/\text{He}/\text{Ar} \rightarrow ^{13}\text{CO}_2/\text{H}_2/\text{He}$). The slopes differ more at initial times than at longer times. This informs us that the bridge formate barrier is time-dependent, which is characteristic of transport phenomenon. (c-d) Indeed, the Arrhenius plot derived from linear fitting of bridge formate semilogarithmic transient curve shown in (b), within the time domain of (c) 1-2 min and (d) 10-20 min demonstrates the time dependency. The time-dependent barrier of bridge formate is diagnostic of transport phenomenon. (e) IR spectra recorded after cooling from 150 °C to 25 °C under D₂/¹²CO₂/He, purging under D₂/He flow for 30 min (D₂ (25 °C)), and switching to O₂/He flow (O₂ (25 °C)) for 2 min. Admittance of O₂ caused the selective removal of monodentate formate, while bridge formate was unaffected. Since we expect oxygen activation to occur on Pd, the selective removal provides spatial information about the two formates. Specifically, monodentate is near to Pd—likely stabilized through hydrogen bonding—whereas bridge formate resides further away. (f) Variable temperature IR spectra under D₂/He following treatment in (e). The experiment demonstrates that monodentate and bridge formate interconvert on the oxide surface via diffusion. (g) Arrhenius plot for monodentate and bridge formate obtained during isotopic switching experiments ($^{12}\text{CO}_2/\text{H}_2/\text{He}/\text{Ar} \rightarrow ^{13}\text{CO}_2/\text{H}_2/\text{He}$). The barrier for

monodentate formate removal is higher than the barrier for bridge formate removal. This is consistent with diffusion of bridge formate (a physical process) to monodentate sites, followed by monodentate formate dehydrogenation (a chemical process). (h) Normalized ^{12}CO mass signals during isotopic switching at 300 °C. (i) Time constants for ^{12}CO (τ_{CO}) obtained upon integration of the (non)-steady-state transients shown in (h). The τ_{CO} value for the $^{12}\text{CO}_2 + \text{H}_2 \rightarrow ^{13}\text{CO}_2 + \text{H}_2$ steady-state transient represents the *upper* limit under constant coverage and temperature. The τ_{CO} value for the $^{12}\text{CO}_2 + \text{H}_2 \rightarrow \text{He}$ non-steady-state transient represents the *lower* limit under constant temperature. Therefore, the τ_{CO} values during the other two non-steady state transients reflect the lifetime of the active surface species derived from the missing gas-phase component. Thus, hydrogen is a long-lived surface specie. The data for Pd/CeO₂-Al₂O₃ is qualitatively and quantitatively (in the case of formate barriers) identical to our previous work using Pd/Al₂O₃.¹¹ Therefore, the mechanistic conclusions from Pd/Al₂O₃ are applicable to Pd/CeO₂-Al₂O₃.

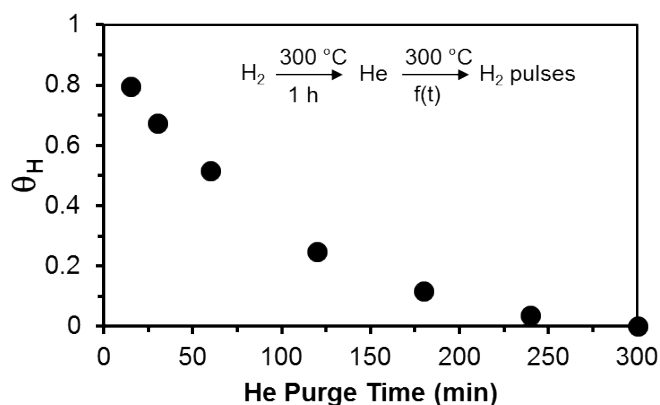


Figure S12. The relative H-coverage (θ_H) as a function of He purge time. θ_H is calculated assuming (incorrectly) that after 300 min He purge there is no hydrogen on the surface of the catalyst. So,

$$\theta_H = \frac{\text{H}_2 \text{ consumed after 300min He purge} - \text{H}_2 \text{ consumed after X min He purge}}{\text{H}_2 \text{ consumed after 300min He purge}}$$

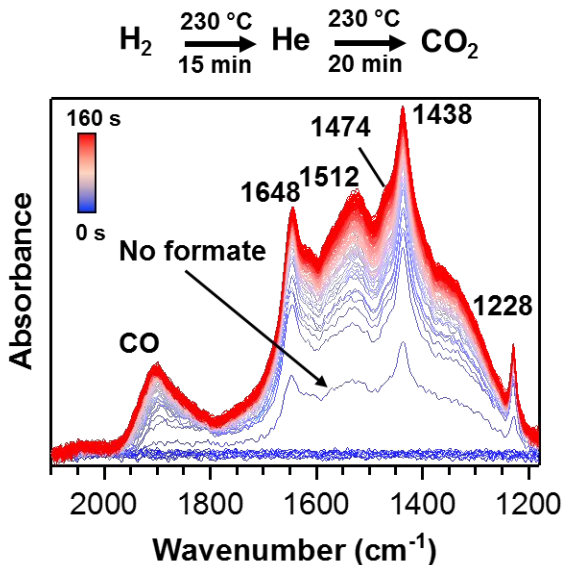


Figure S13. IR spectra recorded following the gas sequence above the figure. The 20 minute He purge removes all gas phase hydrogen from the system. Admittance of CO_2 to the catalysts results in carbonyl formation in the absence of formate (1590 cm^{-1}). In contrast, formate is observed in the presence of H_2 (Figure S6). The results are also observed for $\text{Pd}/\text{Al}_2\text{O}_3$.¹¹ Bicarbonate bands are observed at 1648 [$\nu(\text{OCO})_{\text{asym}}$], 1474 [$\nu(\text{OCO})_{\text{sym}}$], 1438 [$\nu(\text{OCO})_{\text{sym}}$], and 1228 [$\gamma(\text{COH})$] cm^{-1} .^{6,7} The band at 1512 cm^{-1} is attributed to a carbonate.⁶

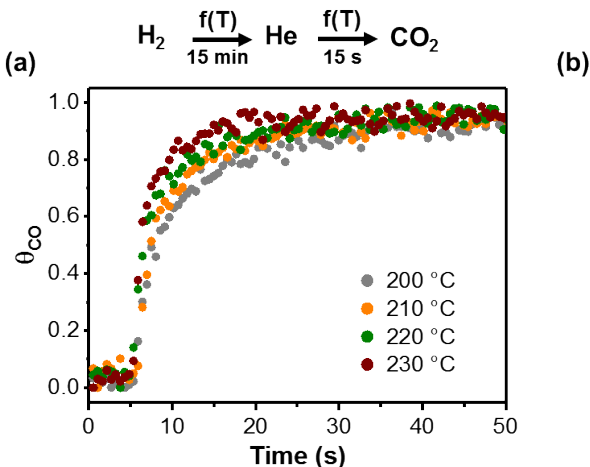


Figure S14. (a) Normalized carbonyl absorbance at 1890 cm^{-1} (θ_{CO}) as a function of CO_2 exposure time beginning at $t = 5 \text{ s}$ using the gas sequence above the plot. The individual data sets were integrated to find τ_{CO} . Three separate experiments were conducted and the average τ_{CO} is reported in (b) along with the pseudo-first-order rate constant ($\tau_{\text{CO}}^{-1} = k_{\text{CO}}$) used for the Arrhenius plot in Figure 2b. The errors represent standard deviation. The catalyst was treated in O_2 at $350 \text{ }^\circ\text{C}$ prior to each experiment.

(a)

Time (min) ^a	Catalyst ^b	MS ^c
-29 < t < 2	H ₂	H ₂
2 < t < 2.4	He (bypass)	H ₂
2.4 < t < 8	He (bypass)	CO ₂
8 < t < 11	CO ₂	CO ₂
11 < t < 11.4	He (bypass)	CO ₂
11.4 < t < 15	He (bypass)	H ₂
15 < t < 21	H ₂	H ₂
21 < t < 25	He (bypass)	H ₂

^aCorresponds to time on MS plot. ^bThe gas that the catalyst is exposed during time, t. ^cThe gas the MS sees during time, t.

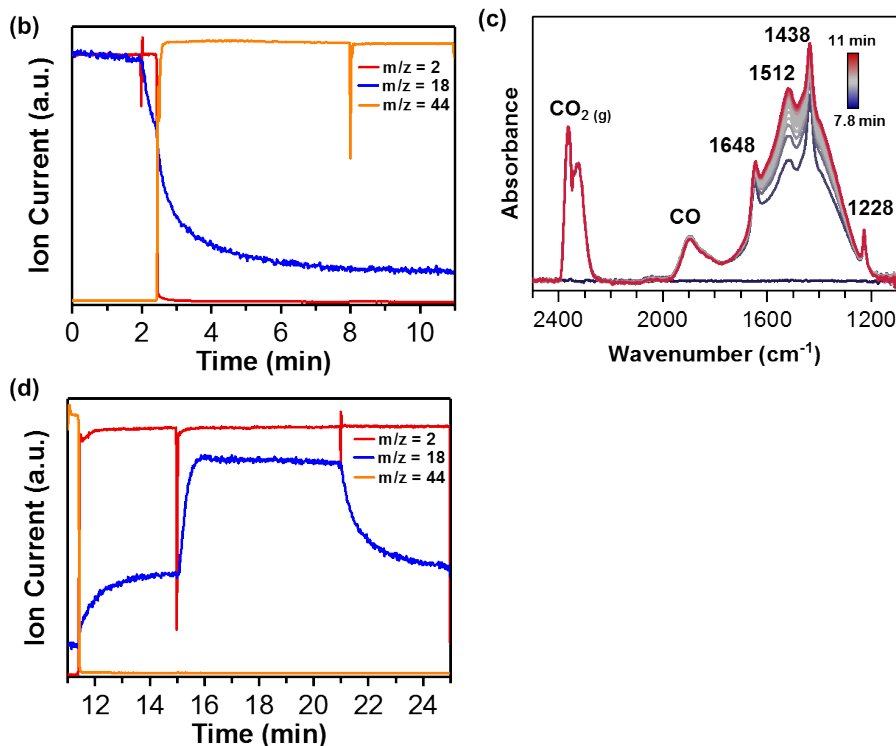


Figure S15. (a) Table showing the type of gas the catalyst and MS are exposed to at time t on the MS plots. (b) MS plot showing the absence of water evolution when exposing the H₂-activated catalyst to CO₂ at $t = 8$ min. The pre-existing water signal ($m/z = 18$) is due to residual water in the hydrogen gas. (c) IR spectra showing the formation of carbonyl when exposing the H₂-activated catalyst to CO₂ at $t = 8$ min. Bicarbonate bands are observed at 1648 [$\nu(\text{OCO})_{\text{asym}}$], 1438 [$\nu(\text{OCO})_{\text{sym}}$], and 1228 [$\gamma(\text{COH})$] cm^{-1} .^{6,7} The band at 1512 cm^{-1} is attributed to a carbonate.⁶ (d) MS plot showing the formation of water when exposing the carbonyl-containing catalyst to H₂ at $t = 15$ min. The water signal likely contains contributions from carbonyl methanation and from hydrogenation of adsorbed hydroxyl, i.e. the byproduct of the CO₂ to carbonyl conversion. This experiment demonstrates that, *if present*, we should be able to detect water formation upon introduction of CO₂ to the H-activated catalyst at $t = 8$ min. Thus, the experiment indicates that COOH dissociates to adsorbed CO and OH (i.e. no water formation).

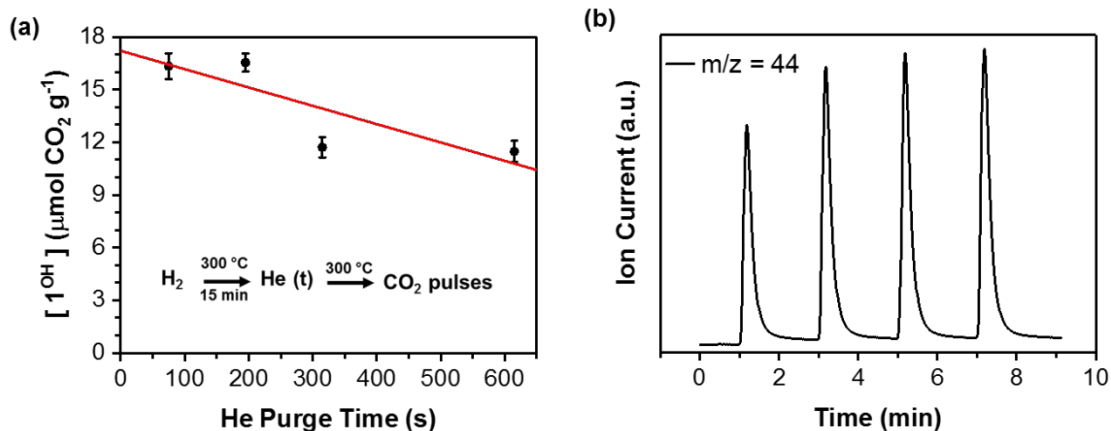


Figure S16. (a) The true number of intermediates $[1^{\text{OH}}]$ for Pd/CeO₂-Al₂O₃ as a function of He purge time obtained via CO₂ pulse titration. The catalyst was treated with H₂ for 15 min at 300 °C, followed by purging with He for various times, and pulse introduction of CO₂. The 1^{OH} values are calculated using 1:1 stoichiometry with the moles of CO₂ consumed during pulse titration. The value reported in Table 2 corresponds to the y-intercept of the best fit line (red). Each data point is the average of four experiments and the error bars represent standard deviation. (b) Representative pulse CO₂ data used to derive the $[1^{\text{OH}}]$ values. For Pd/Al₂O₃, the $[1^{\text{OH}}]$ value is derived from four data points at a 75 s He purge. As can be seen from (a), the data point at 75 s (16.3 ± 0.7) is statistically identical to the y-intercept (17.2 ± 1.9). Thus, the $[1^{\text{OH}}]$ value for Pd/Al₂O₃ obtained at 75 s He purge is likely to be equivalent to the value extrapolated to 0 s He purge.

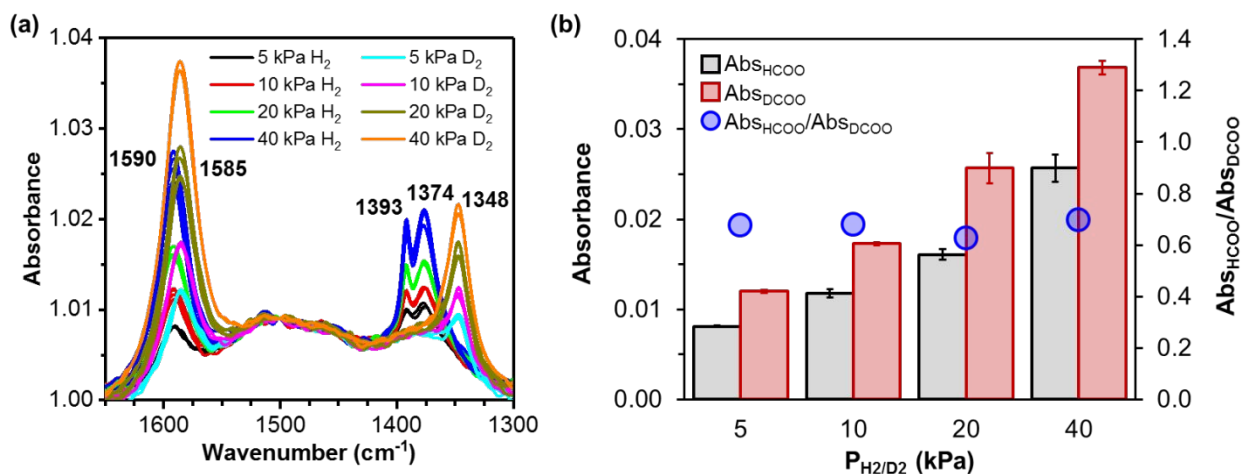


Figure S17. (a) IR data collected at 300 °C after treating Pd/CeO₂-Al₂O₃ with H₂ or D₂ for 10 min, followed by a step-function switch to CO₂ for 1 min, and then a step-function switch back to H₂ or D₂ (i.e. H₂/D₂ → CO₂ → H₂/D₂). This procedure was done as a function of H₂/D₂ pressure with three data sets for each pressure (except for '40 kPa D₂' which only has two data sets). The first IR spectrum was recorded concurrent with the switch back to H₂/D₂ (i.e. CO₂ → H₂/D₂), $t = 0$ s, and recorded thereafter every 20 s for 160 s. The spectra shown here correspond to those collected at $t = 60$ s. Prior to each experiment, residual formate was removed by annealing under He at 300 °C until the formate band was no longer present in the IR spectrum. This is critical for relating formate absorbance to H/D coverage. H-Formate bands are observed at 1590 [$\nu(\text{OCO})_{\text{asym-br}}$], 1393 [$\delta(\text{CH})$], and 1374 [$\nu(\text{OCO})_{\text{sym-br}}$] cm⁻¹.⁸⁻¹⁰ D-Formate

bands are observed at 1585 [$\nu(\text{OCO})_{\text{asym-br}}$] and 1348 [$\nu(\text{OCO})_{\text{sym-br}}$] cm^{-1} . (b) The left axis shows the absorbance of the formate band at 1590 cm^{-1} (Abs_{HCOO}) and 1585 cm^{-1} (Abs_{DCOO}) as a function of H_2/D_2 pressure derived from the spectra in (a). The right axis shows the ratio between the Abs_{HCOO} and Abs_{DCOO} value as a function of H_2/D_2 pressure, where the average is $\text{Abs}_{\text{HCOO}}/\text{Abs}_{\text{DCOO}} = 0.67 \pm 0.02$. The value in Table 3, Entry EIE is the average of the $\text{Abs}_{\text{HCOO}}/\text{Abs}_{\text{DCOO}}$ ratio determined from the spectra collected at $60 \text{ s} \leq t \leq 160 \text{ s}$, i.e. the average of six sets of spectra or 18 data points.

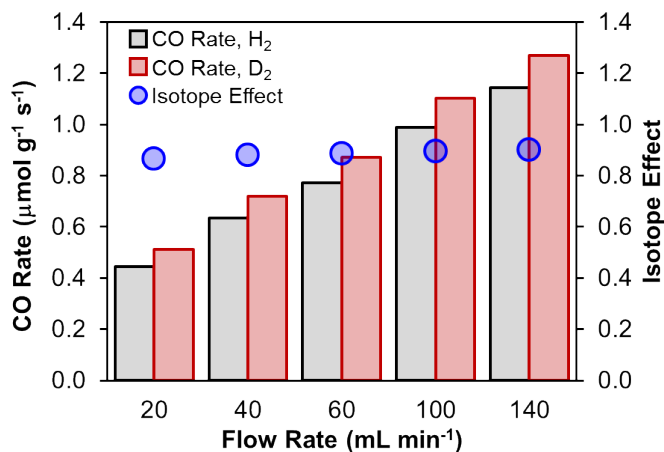


Figure S18. CO formation rate (r) during rWGS using H_2 (H) or D_2 (D) as a function of total flow rate (left axis). The right axis shows the observed isotope effect (IE) as a function of total flow rate, with an average $\text{IE} = r_{\text{H}}/r_{\text{D}} = 0.89 \pm 0.01$. Conditions: $\text{Pd}/\text{Al}_2\text{O}_3 = 14.5 \text{ mg}$, $\gamma\text{-Al}_2\text{O}_3 = 36.2 \text{ mg}$, $V_{\text{bed}} = 0.066 \text{ mL}$, $T = 300 \text{ }^\circ\text{C}$, $\text{CO}_2:4\text{H}_2:15\text{He}$.

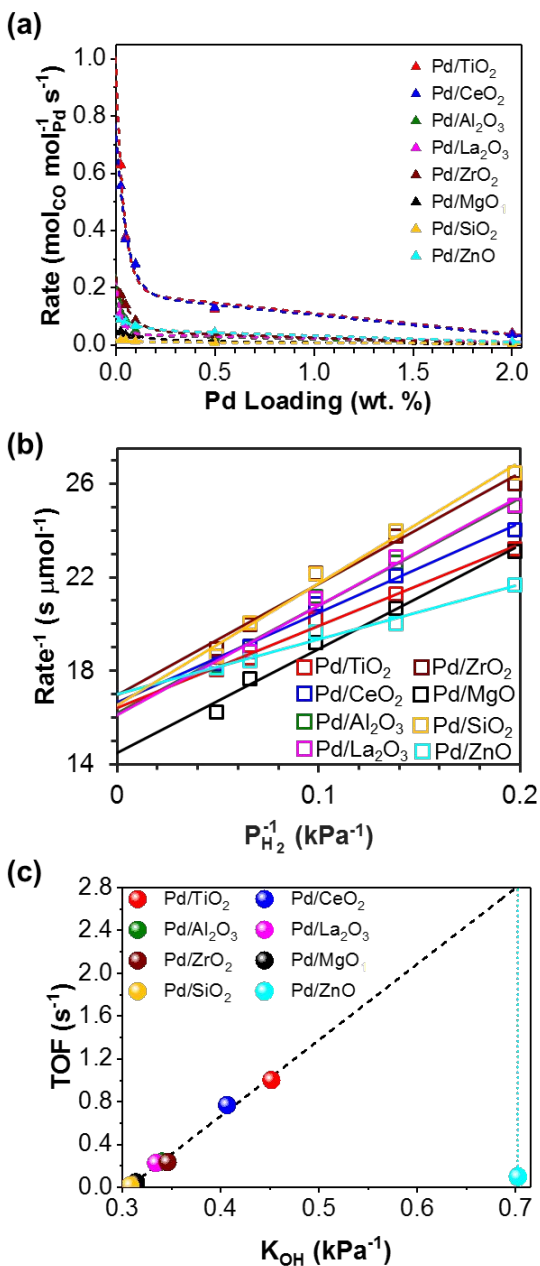


Figure S19. (a) rWGS rate at 300 °C as a function of Pd loading. (b) Response of the rWGS rate to changes in the partial pressure of hydrogen fit to eq 5. (c) Plot of the rWGS turnover frequency as a function of the equilibrium constant for hydroxyl formation.

The method in Figure 3a, S19a only provides a proxy for the TOF, i.e. it is an apparent TOF. It cannot account for Pd-Zn alloy formation¹² under reaction conditions, and therefore, underestimates the true TOF. That is, the Pd/ZnO catalyst initially has a fixed number of active sites, which we define as the moles of Pd. If Pd-O-Zn (the true active site) goes to Pd-Zn (alloy formation) via eq 6, then the number of active sites is reduced by one. The true TOF would not change. However, the apparent TOF (i.e. the one determined via Figure 3a) is now an underestimation because the number of active sites is defined by the moles of Pd and not the number of Pd-O-Zn sites. In other words, the rate decreases due to the loss of an

active site, but this is not counteracted by a decrease in site concentration using the method to determine the apparent TOF.

References

- (1) Koros, R. M.; Nowak, E. J. A diagnostic test of the kinetic regime in a packed bed reactor. *Chem.Eng.Sci.* **1967**, *22*, 470.
- (2) Yang, Y.; Disselkamp, R. S.; Szanyi, J.; Peden, C. H. F.; Campbell, C. T.; Goodwin, J. G. Design and operating characteristics of a transient kinetic analysis catalysis reactor system employing in situ transmission Fourier transform infrared. *Rev.Sci.Instrum.* **2006**, *77*, 094104.
- (3) Wuttke, S.; Bazin, P.; Vimont, A.; Serre, C.; Seo, Y.-K.; Hwang, Y. K.; Chang, J.-S.; Férey, G.; Daturi, M. Discovering the Active Sites for C3 Separation in MIL-100(Fe) by Using Operando IR Spectroscopy. *Chem.Eur.J.* **2012**, *18*, 11959-11967.
- (4) Shannon, S. L.; Goodwin, J. G. Characterization of catalytic surfaces by isotopic-transient kinetics during steady-state reaction. *Chem.Rev.* **1995**, *95*, 677-695.
- (5) Ledesma, C.; Yang, J.; Chen, D.; Holmen, A. Recent approaches in mechanistic and kinetic studies of catalytic reactions using SSITKA technique. *ACS Catal.* **2014**, *4*, 4527-4547.
- (6) Szanyi, J.; Kwak, J. H. Dissecting the steps of CO₂ reduction: 1. The interaction of CO and CO₂ with [gamma]-Al₂O₃: an in situ FTIR study. *Phys.Chem.Chem.Phys.* **2014**, *16*, 15117-15125.
- (7) Szanyi, J.; Kwak, J. H. Dissecting the steps of CO₂ reduction: 2. The interaction of CO and CO₂ with Pd/[gamma]-Al₂O₃: an in situ FTIR study. *Phys.Chem.Chem.Phys.* **2014**, *16*, 15126-15138.
- (8) Rubasinghege, G.; Ogden, S.; Baltrusaitis, J.; Grassian, V. H. Heterogeneous uptake and adsorption of gas-phase formic acid on oxide and clay particle surfaces: The roles of surface hydroxyl groups and adsorbed water in formic acid adsorption and the impact of formic acid adsorption on water uptake. *J. Phys.Chem. A* **2013**, *117*, 11316-11327.
- (9) Deacon, G. B.; Phillips, R. J. Relationships between the carbon-oxygen stretching frequencies of carboxylato complexes and the type of carboxylate coordination. *Coord.Chem.Rev.* **1980**, *33*, 227-250.
- (10) Tong, S. R.; Wu, L. Y.; Ge, M. F.; Wang, W. G.; Pu, Z. F. Heterogeneous chemistry of monocarboxylic acids on alpha-Al₂O₃ at different relative humidities. *Atmos.Chem.Phys.* **2010**, *10*, 7561-7574.
- (11) Nelson, N. C.; Nguyen, M.-T.; Glezakou, V.-A.; Rousseau, R.; Szanyi, J. Carboxyl intermediate formation via an in situ-generated metastable active site during water-gas shift catalysis. *Nat.Catal.* **2019**, *2*, 916-924.
- (12) Tew, M. W.; Emerich, H.; van Bokhoven, J. A. Formation and Characterization of PdZn Alloy: A Very Selective Catalyst for Alkyne Semihydrogenation. *J.Phys.Chem. C* **2011**, *115*, 8457-8465.